Computation Guided Design of $LiTaSiO_5$, a New Lithium Ionic Conductor with Sphene Structure

Shan Xiong, Xingfeng He, Aijie Han, Zhantao Liu, Zhensong Ren, Brian McElhenny, Adelaide M Nolan, Shuo Chen, Yifei Mo*, and Hailong Chen**

S. Xiong, A. Han, Z. Liu, Prof. H. Chen

The Woodruff School of Mechanical Engineering

Georgia Institute of Technology

Atlanta, GA 30332, U.S.

E-mail: hailong.chen@me.gatech.edu

X. He, A. M. Nolan, Prof. Y. Mo

Department of Materials Science and Engineering

University of Maryland

College Park, MD 20742, U.S.

E-mail: yfmo@umd.edu

Z. Ren, B. McElhenny, Prof. S. Chen

Department of Physics and Texas Center for Superconductivity

University of Houston

Houston, TX 77204, U.S.

E-mail: schen34@uh.edu

This is the author manuscript accepted for publication and has undergone full peer review but has not been through the copyediting, typesetting, pagination and proofreading process, which may lead to differences between this version and the Version of Record. Please cite this article as doi: 10.1002/aenm.201803821.

Keywords: solid electrolytes, solid-state batteries, lithium superionic conductors, first principles calculations

The development of all-solid-state Li-ion batteries requires solid electrolyte materials with many desired properties, such as ionic conductivity, chemical and electrochemical stability, and mechanical durability. Computation-guided materials design techniques are advantageous in designing and identifying new solid electrolytes that can simultaneously meet these requirements. In this joint computational and experimental study, we successfully identified, synthesized and demonstrated a new family of fast lithium ion conductors, namely $LiTaSiO_5$ with sphene structure, using a novel computational design strategy. First-principles computation predicted that Zr-doped $LiTaSiO_5$ sphene materials have fast Li diffusion, good phase stability, and poor electronic conductivity, which are ideal for solid electrolytes. Experiments confirmed that Zr-doped $LiTaSiO_5$ sphene structure indeed exhibit encouraging ionic conductivity. The lithium diffusion mechanisms in this material were also investigated, indicating the sphene materials are 3-D conductors with facile 1-D diffusion along the [101] direction and additional cross-channel migration. This study demonstrated a novel design strategy of activating fast Li ionic diffusion in lithium sphenes, a new materials family of superionic conductors.

1. Introduction

All-solid-state Li-ion batteries (ASLiBs) with inorganic solid electrolytes (SEs) are considered one of the most promising alternatives to current Li-ion batteries (LIBs), which use organic liquid electrolytes, as ASLiBs offer enhanced safety, wide operating temperature range, and potentially high energy density if combined with Li-metal anodes.[1-4] As the key enabler of ASLiBs, solid state Li-ion conductors with high Li ionic conductivity, a wide electrochemical window, and good chemical stability are highly desirable. Despite significant research efforts in the past decades, out of thousands of known lithium-containing inorganic compounds, only a limited number of materials have been identified as superionic conductors with Li^+ conductivities comparable to conventional liquid electrolyte (~1-10 $mS \cdot cm^{-1}$ at room temperature), including $Li_{10}GeP_2S_{12}$ (LGPS),[5] $Li_7P_3S_{11}$,[6] garnet $Li_7La_3Zr_2O_{12}$ (LLZO),[7, 8] and LISICON $Li_{1.3}Al_{0.3}Ti_{1.7}(PO_4)_3$ (LATP).[9] However, many of these superionic conductors suffer from limited stability either in the air or against Li metal.[4, 10-12] Therefore, it is still necessary to explore, discover, and design new compounds with both high ionic conductivity and outstanding stability as solid electrolytes for ASLiBs.

In the past, the design and discovery of Li ionic conductors have been largely based on trial-and-error, due to the limited understanding of ionic conductivity in existing super-ionic conductors. A general design strategy for fast ion conduction can be tremendously helpful yet is currently absent. Recently, computational studies by Mo *et al* [13] revealed that the fast ion diffusion in Li super-ionic conductors can occur through concerted migration of multiple Li ions, where the migration of high-energy-site Li ions effectively reduces the energy barrier. Based on this understanding, Mo *et al* proposed a general design strategy to drastically lower the energy barriers by intentionally inducing Li ions into high energy sites to activate the concerted migration of multiple ions.[13] The rationale of this design strategy may explain the increase of Li ionic conductivity in a number of existing Li ion conductors.[13] The ion conductivity of garnet $Li_7La_3Zr_2O_{12}$ (LLZO) can achieve 0.1 - 1 $mS \cdot cm^{-1}$ after inserting additional Li into the original garnet $Li_5La_3M_2O_{12}$ (M=Ta, Nb) or $Li_3Ln_3Te_2O_{12}$ (Ln=Y, Pr, Nd, Sm–Lu), which exhibit much lower ionic conductivity (<10^{-3} $mS \cdot cm^{-1}$).[7] The increase of the conductivity of LISICON $Li_{1+x}Al_xTi_{2-x}(PO_4)_3$ when increasing the Li amount from 1 to 1.2-1.3 can also be explained by this mechanism.[9, 14] This design strategy has yet to be demonstrated in predicting a new material system with high ionic conductivity.

Here, through a combined computational and experimental study, the proposed design strategy was demonstrated to activate concerted migration in a new family of materials, lithium sphene. The sphene compounds, with the general formula $ABXTO_4$ (A = Li, Na or Ca, etc., B = Ti, Ta or other metals, X=O or F, T=Si, Ge, P, or S, etc.), is a well-known large materials family,[15, 16] but has rarely been explored for ionic conduction properties. $LiTaSiO_5$ is a known sphene compound[17] with a crystal structural framework comprising of corner-sharing TaO_6 and SiO_4 polyhedrons (**Figure 1**a). Li ions located at 4e tetrahedral sites are bonded with 4 oxygen ions, and the LiO_4 tetrahedrons share edges to neighboring TaO_6 and SiO_4 polyhedrons. The crystal structural framework of $LiTaSiO_5$ has lithium diffusion channels of decent size and a well-connected Li^+ percolation network, but has not yet been studied for Li^+ transport.

In this study, we first evaluated the structures and properties of $LiTaSiO_5$ using first principles computation. Following the aforementioned design strategy proposed by Mo *et al.*,[13] we computationally designed $Li_{1+x}Ta_{1-x}Zr_xSiO_5$ through aliovalent doping of Zr at the Ta sites in $LiTaSiO_5$ to insert Li into the high-energy sites (as charge compensation) and thus to activate low-barrier concerted migration in the lattice. Then we experimentally synthesized a series of $Li_{1+x}Ta_{1-x}Zr_xSiO_5$ compounds and measured their ionic conductivities. The experiments indeed demonstrated $Li_{1+x}Ta_{1-x}Zr_xSiO_5$ can achieve a significantly lower activation energy of 0.38 eV and a high conductivity of >0.01 $mS\cdot cm^{-1}$ at room temperature. This suggests our computationally guided rational design has led to the discovery of a new family of promising Li ionic conductors.

2. Results

2.1 Computational Results

2.1.1 Crystal Structure

We performed topological analysis of the crystal structural framework of $LiTaSiO_5$ to determine the Li diffusion channels and potential space to accommodate more Li ions. The topological analysis identified three Li sites that are large enough to accommodate Li ions. Consistent with previously experimentally identified Li sites in $LiTaSiO_5$,[17] the Li1 site was identified as the largest space for Li ions (**Figure 1**). Two octahedral sites, Li2 and Li3, neighboring the Li1 site (**Figure 1**b), were identified as potential new Li interstitial sites with smaller size. More Li ions could be inserted into these Li2 and Li3 sites if aliovalent doping is applied, as a mechanism of charge compensation (i.e., the use of a 4+ cation to substitute the Ta^{5+}). It is important to note that the Li2 and Li3 sites are located in the middle of two neighboring Li1 sites. The connection through these alternating Li1, Li2, and Li3 sites forms a well-connected 1D Li diffusion channel along the [101] direction (**Figure 1**b). This 1D diffusion channel with alternating sites is similar to the 1D Li diffusion channel in $Li_{10}GeP_2S_{12}$ (LGPS). These Li sites and diffusion channels with low barriers were confirmed by DFT calculations and AIMD simulations.

2.1.2 Phase Stability

Following the design strategy of inducing concerted migration by Mo *et al*,[13] in the computational model we inserted extra Li into these Li2 and Li3 interstitial sites through doping of Zr^{4+} at Ta^{5+} sites, and created the composition $Li_{1+x}Ta_{1-x}Zr_xSiO_5$. The DFT calculations confirmed the crystal structural stability and the predicted interstitial sites in the compositions of $Li_{1+x}Ta_{1-x}Zr_xSiO_5$ at $x = 0.125$, 0.25, and 0.5. After DFT relaxation the sphene structure remains with little distortion. The relaxed positions of newly inserted Li ions agreed with the newly predicted Li2 and Li3 sites (**Figure 1**), with local relaxation of less than 0.3 Å from the original predicted positions. The Li ions at Li1 sites also exhibited small local relaxation to compensate the strong Li-Li interactions due to Li insertion. The volume of the unit cell of $Li_{1+x}Ta_{1-x}Zr_xSiO_5$ at $x = 0.125$, 0.25, and 0.5 was increased by 0.9%, 1.9%, and 3.6% compared to pristine $LiTaSiO_5$ (**Table S2** in SI). All these compositions have good phase stability as evaluated using the phase diagrams based on DFT energies from the *Materials Project*.[18] $LiTaSiO_5$ is a thermodynamically stable phase. All doped compositions of $Li_{1+x}Ta_{1-x}Zr_xSiO_5$ at $x = 0.125$, 0.25, and 0.5 have relatively small energies above the hull of 11, 15, and 28 meV per atom, respectively, as determined via the decomposition reaction

$$Li_{1+x}Ta_{1-x}Zr_xSiO_5 \text{ -> } (1-x)\ LiTaSiO_5 + x\ ZrO_2 + x\ Li_2SiO_3$$

These small values of energy above hull suggest good phase stability of the sphene structure upon Zr doping and Li insertion.

2.1.3 Electronic structure

The band gap calculated using the HSE functional was 5.3 eV, 4.8 eV and 5.4 eV for $Li_{1+x}Ta_{1-x}Zr_xSiO_5$ at $x = 0$, 0.25, and 0.5, respectively (**Figure 2**). The large band gap indicates the poor electronic conductivity of $Li_{1+x}Ta_{1-x}Zr_xSiO_5$, which agrees well with experimental observations. The introduction of Zr dopants and Li interstitials did not have a significant effect on the value of the band gap, nor introduce any new defect states within the band gap (**Figure 2**).

2.1.4 Thermodynamic intrinsic electrochemical window

Thermodynamic analyses were performed to evaluate the thermodynamic intrinsic window of $LiTaSiO_5$, which is an important property of solid electrolytes in all-solid-state Li-ion batteries.

$LiTaSiO_5$ shows a decent electrochemical window with a thermodynamic intrinsic anodic limit of 3.96 V (referenced to Li/Li$^+$), indicating its good stability at high voltage. However, $LiTaSiO_5$ is not thermodynamically stable against Li metal and has a thermodynamic intrinsic cathodic limit of 1.40 V (referenced to Li/Li$^+$). The reduction of Ta and Si limits the Li metal stability of $LiTaSiO_5$.[12]

2.1.5 Li$^+$ Diffusion mechanism

AIMD simulations were performed for $Li_{1+x}Ta_{1-x}Zr_xSiO_5$ compositions to evaluate their Li$^+$ diffusivity. For all $Li_{1+x}Ta_{1-x}Zr_xSiO_5$ compositions, the Li diffusivities evaluated at different temperatures follow an Arrhenius relationship (**Figure 3**). The stoichiometric composition $LiTaSiO_5$ shows very low Li$^+$ diffusion with a high activation energy of 0.70 eV and an extrapolated conductivity of 7.6×10^{-7} mS·cm^{-1} at 300K (**Table 1**). The predicted slow Li diffusion at room temperature is consistent with our experimental observations.

Compared with $LiTaSiO_5$, $Li_{1+x}Ta_{1-x}Zr_xSiO_5$ compositions have greatly increased Li conductivities of 1.5, 6.1, and 6.3 mS·cm^{-1} at 300 K for x = 0.125, 0.25, and 0.5, respectively. The activation energies also decrease to 0.25, 0.21, and 0.23 eV for x = 0.125, 0.25, and 0.5, respectively (**Table 1** and **Figure 3**). These predicted conductivities for $Li_{1+x}Ta_{1-x}Zr_xSiO_5$ at 300K are comparable to the best existing oxide Li ionic conductors, such as doped garnet LLZO (0.1 to 1 mS·cm^{-1}). In addition, we observed that the concerted migration of multiple Li ions with lower migration barriers was activated at x = 0.125 - 0.5 during our AIMD simulations (**Figure S2**), consistent with the proposed design strategy. The Li2 and Li3 sites, where new Li ions were inserted, have higher energy in the energy landscape than Li1 sites. As a result, in $Li_{1+x}Ta_{1-x}Zr_xSiO_5$, the activated concerted migrations exhibit a significantly lower energy barrier of 0.21 to 0.25 eV, compared to 0.7 eV in pristine $LiTaSiO_5$. This decrease in activation energy greatly increases the Li conductivity by several orders of magnitude as observed in AIMD simulations.

AIMD simulations also revealed the Li ion diffusion mechanism in $Li_{1+x}Ta_{1-x}Zr_xSiO_5$ at different Li concentrations of 1+x. The spatial occupancy density of Li ions in $Li_{1+x}Ta_{1-x}Zr_xSiO_5$ at x = 0 and 0.25 is shown in **Figure 4**. We found that the stoichiometric $LiTaSiO_5$ shows a 1D percolating diffusion channel along the [101] direction, in agreement with our topological structural analysis. There is a large region of Li density at Li1 sites, corresponding to a large space for accommodating Li, and a flat energy landscape for Li migration. In $Li_{1+x}Ta_{1-x}Zr_xSiO_5$ with $x \geq 0.125$, the [101] diffusion channel connecting Li1-Li3 sites is still the fastest Li diffusion channel. In addition, the diffusion across these [101] channels is activated, as shown by the Li spatial occupancy density (**Figure 4**b). Therefore, $Li_{1+x}Ta_{1-x}Zr_xSiO_5$ is a 3D Li-ion conductor with fast 1D diffusion channels, similar to LGPS.[19, 20]

2.2 Experimental Results

2.2.1 Crystal Structure and Microstructure Characterizations

Based on the computational results, a minimum amount of 12.5% Zr-doping is required to achieve a conductivity over 0.1 $mS \cdot cm^{-1}$. On the other hand, the computational results also indicate that when the Zr-doping exceeds 25%, the energy above hull will greatly increase to above 15 meV/atom, suggesting that a doping level of >25% may be difficult to achieve experimentally. The syntheses of the solid solution series with various Zr-doping levels within the predicted solubility range (12.5%, 20%, 25%, 30%, and 50%) were attempted and the composition and crystal structures were examined by powder X-ray diffraction (XRD).

$Li_{1+x}Ta_{1-x}Zr_xSiO_5$ samples were prepared with x = 0, 0.125, 0.20, 0.25, 0.30, and 0.50, respectively, with solid state synthesis method. The starting materials were mixed using high energy ball-milling and the pellets of the samples were sintered at 1100 °C between 24 and 48 hours. The XRD patterns of the samples are shown in **Figure 5**a. The as-synthesized undoped $LiTaSiO_5$ was in good agreement with PDF#77-0896. The doped sample $Li_{1.125}Ta_{0.875}Zr_{0.125}SiO_5$ (x=0.125) shows a very similar XRD pattern with a small amount of $LiTaO_3$ impurity formed in the heating process. Compared with the pattern of undoped $LiTaSiO_5$, major peaks of the 12.5% Zr-doped sample, such as ones at $2\theta = 8.2°, 10.3°, 12.2°, \text{and } 12.7°$, etc., slightly shift toward lower two-theta angles, indicating an expansion of the unit cell. This indicates that most Zr from the starting materials dopes into the $LiTaSiO_5$ lattice at the Ta sites, despite the formation of the very minor amounts of the secondary phase. The increased unit cell volume is expected due to the replacement of the smaller sized Ta^{5+} by large Zr^{4+} in the lattices.

For the samples with higher doping levels (x > 0.2), the primary phase with the $LiTaSiO_5$ structure was still obtained in all the samples, with the reflections shifting towards lower two-theta angles as the amount of Zr in the starting materials increased. However, evident impurity of $LiTaO_3$ (or $Li_{1+x}Ta_{1-x}Zr_xO_3$) was also observed, and the fraction of the impurity increased greatly as the amount of Zr in the starting materials increased. For samples with 30% and 50% Zr-doping (x = 0.3 and 0.5), a longer synthesis time, up to 48 hours, was attempted to convert the impurity to the target phase, but the purity did not obviously improve. This implies that the formation of the impurities is not due to the slow reaction kinetics but more likely due to the thermodynamic instability of the desired composition. It is also worth noting that obvious softening and partial melting of the pellets were observed with increasing amounts of ZrO_2 added to the starting materials.

Synchrotron XRD patterns and the corresponding Rietveld refinement results of both undoped and 12.5% Zr-doped $LiTaSiO_5$ are shown in **Figure 5**b and c, respectively. For the undoped sample, the refinement results confirmed the formation of the primary $LiTaSiO_5$ phase with a space group of $P12_1/c1$(No. 14) and the lattice parameters were refined to a = 7.3973(2) Å, b=7.9308(7) Å, and c=7.4444(5) Å, β=119.15°. The impurity $LiTaO_3$ phase was also identified with a space group of $R3c$ (No. 161) and the phase weight fraction was estimated to be less than 4% based on the refinement results. The primary phase of 12.5% Zr-doped sample ($Li_{1.125}Ta_{0.875}Zr_{0.125}SiO_5$) was refined using the same space group of $P12_1/c1$(No. 14) with 12.5% Ta sites occupied by Zr and accordingly with additional Li at Li sites predicted by the computation. The lattice parameters of the primary phase were refined to a = 7.3485(3) Å, b=7.9937(1) Å, and c=7.4298(9) Å, β=118.41°. The unit cell volume of the 12.5% Zr-doped sample increased by 0.64% compared with the undoped sample, which is consistent with the computational results and the fact that the ionic radius of Zr^{4+} (0.72 Å) is slightly larger than that of Ta^{5+} (0.64 Å). The secondary impurity, the $LiTaO_3$ phase, refined with a space group of $R3c$ (No. 161), was estimated to be less than 5% in the 12.5% Zr-doped $LiTaSiO_5$ sample. The crystallographic details extracted from the Rietveld refinement results are summarized in **Table S1**. These results are also confirmed by Rietveld refinement of the same samples based on neutron diffraction data, which were shown in **Figure S3.** HR-TEM image and electron diffraction were taken for the 12.5% Zr doped sample, as shown in **Figure S4** in the supplementary information. The electron diffraction patterns are consistent with the crystal structure determined by X-ray and neutron diffractions.

Scanning electron microscope (SEM) was used to investigate the morphology of $Li_{1+x}Ta_{1-x}Zr_xSiO_5$ samples. **Figure 6** shows the scanning electron microscope (SEM) images for the synthesized $Li_{1.125}Ta_{0.875}Zr_{0.125}SiO_5$ (x=0.125) powder and hot-pressed pellets. For the as-synthesized powder, the particles show irregular shapes and a relatively wide distribution of particle sizes (1~10 µm), which is plausibly due to the melting-quenching process in the synthesis. After hot-pressing, the sample shows smoother surfaces and much higher density with less voids and grain boundaries, as shown in **Figure 6**b. The morphology and density change under hot-press led to tight contact among the particles and reduced grain boundary resistance, which is favorable for conductivity measurements. The SEM image and the corresponding elemental mapping with energy dispersive X-ray (EDX) spectroscopy of $Li_{1.125}Ta_{0.875}Zr_{0.125}SiO_5$ was shown in **Figure S5**. The distribution of Si, Ta, Zr and O elements in the EDX mapping confirms the uniform formation of $Li_{1.125}Ta_{0.875}Zr_{0.125}SiO_5$ with no evident element or phase segregations. The SEM images of both surface and cross section for undoped, 12.5% Zr, and 20% Zr-doped $LiTaZrSiO_5$ pellets are also shown in **Figure S6**. It can be seen that denser pellets are formed after hot pressing, especially for the doped samples. The cross-section images show well-fused particles and reduced grain boundaries, which confirms the effectiveness of the hot-pressing method. The relative densities of the hot-pressed pellets are measured to be 74%, 86%, and 88% for undoped, 12.5% Zr, and 20% Zr doped $LiTaSiO_5$ pellets, respectively. Compared with cold-pressed pellets, densities of which are measured to be below 60%, hot-pressed pellets present better contact among particles, less gain boundaries, and much higher relative densities. Therefore, hot-pressing was used for all three samples for the EIS measurements.

In order to evaluate the chemical stability, an air-stability experiment was conducted by exposing the as-synthesized $Li_{1.125}Ta_{0.875}Zr_{0.125}SiO_5$ ($x = 0.125$) sample in an ambient atmosphere for a reasonably long time. As shown in **Figure S7**, the as-synthesized $Li_{1.125}Ta_{0.875}Zr_{0.125}SiO_5$ presents the $LiTaSiO_5$-like main phase and minor impurity of $LiTaO_3$-like phase. After being exposed in the air for 5 and 12 days, no extra diffraction peaks or distinct peaks changes are observed, indicating good chemical stability of this group of oxide materials against air and moisture. This good stability is also confirmed in first principles computation.

2.2.2 Reaction Mechanism of the Solid-State Synthesis

In order to further explore the kinetics and thermodynamics associated with the formation process of $Li_{1+x}Ta_{1-x}Zr_xSiO_5$ with various Zr-doping levels, *in situ* XRD for synthesis was performed by heating up the pellet of ball-milled precursor in an Anton Paar HTK1200N furnace mounted in the X-ray diffractometer. The temperature was raised from room temperature to 1050 °C with multiple steps and XRD data was collected while the temperature was held constant in each step. Evolution of the XRD patterns from samples with $x = 0$ and 0.2 are shown in **Figure 7**a and b, respectively. *In situ* XRD of 50% Zr-doped sample was also conducted and the patterns are shown **Figure S8** in the supplementary information.

As shown in **Figure 7**a, for the undoped $LiTaSiO_5$ sample, reflections of starting materials (Ta_2O_5 and Li_2CO_3) can be observed at room temperature and remain intact below 600 °C. Peaks of SiO_2 are not seen because amorphous SiO_2 was used as the starting material. When heated to 600 °C, $LiTaO_3$ phase starts to form as a product of the reaction between Ta_2O_5 and Li_2CO_3. The peaks of Ta_2O_5 and Li_2CO_3 gradually decreases when temperature increases and eventually disappear at 850 °C. As the temperature goes up, $LiTaSiO_5$ starts to form at 950 °C as a product of the reaction between $LiTaO_3$ and amorphous SiO_2. The fraction of $LiTaO_3$ decreases as the fraction of $LiTaSiO_5$ increases accordingly, as the temperature further increases to 1050 °C. However, a small amount of $LiTaO_3$ phase still exists, even after cooling down to room temperature. Phase-pure $LiTaSiO_5$ product was obtained in lab synthesis, but not in the *in-situ* XRD experiment, because only a 4-hour dwelling time at 1050°C was used in the *in-situ* XRD experiment, which was not long enough to convert all the $LiTaO_3$ phase into the target $LiTaSiO_5$ phase given the rather slow kinetics of this reaction.

A similar reaction pathway was observed for the 20% Zr-doped sample ($Li_{1.2}Ta_{0.8}Zr_{0.2}SiO_5$, x = 0.2) as shown in **Figure 7**b. The intermediate $LiTaO_3$ phase starts to form at 600°C and the starting materials are all consumed upon reaching 850°C with only $LiTaO_3$ phase being observed. Meanwhile a $LiTaSiO_5$-like phase starts to form at 850°C. The increased background at low angle range implies that the sample may be partially melted. Due to the limited reaction time, only a small amount of a $LiTaSiO_5$-like phase was form during the *in-situ* XRD experiment with a large amount of the $LiTaO_3$ phase remaining in the final product. Evidence of this is seen in the significantly lower peak intensities of the $LiTaSiO_5$-like phase than that of the $LiTaO_3$ phase. While this reaction can be facilitated by longer reaction time in a box furnace, this *in situ* XRD result clearly indicates that with increased amount of Zr in the starting materials, the thermodynamic driving force toward the formation of the $Li_{1+x}Ta_{1-x}Zr_xSiO_5$ solid solution phase becomes much smaller, and accordingly the kinetics of the reaction become significantly more sluggish. This can be further confirmed by the *in situ* XRD results of the 50% Zr doped sample, shown in **Figure S8**, which was performed using a higher ending temperature of 1150 °C. Similarly, the intermediate $LiTaO_3$ phase formed below 600°C. However, the pellet completely melted at 1050 °C, which led to the disappearance of all detectable peaks, even after cooling down to room temperature. Similar phenomenon was also observed during the synthesis process in box furnaces, where the pellets of 30% and 50% Zr-doped samples melted and deformed severely. Only limited amount of $Li_{1+x}Ta_{1-x}Zr_xSiO_5$ phase was obtained even after high temperature calcination at 1200°C for 48 hours. Significant amount of $LiTaO_3$ remained in the final product, as shown in the XRD patterns in **Figure 5**a. This indicates that practically, at least within the experimental conditions we have explored so far, the solubility limit of Zr in $Li_{1+x}Ta_{1-x}Zr_xSiO_5$ phases is below 12.5%. Higher doping amount leads to formation of $LiTaO_3$ and other amorphous impurities.

2.2.3 *Ionic conductivity measurement and proof-of-concept electrochemical testing*

Powder of the undoped, 12.5%, and 20% Zr-doped samples were pressed into pellets at 1100 °C with DC heating for 2 minutes to densify the pellet and reduce the grain boundary resistance. These pellets were then analyzed with EIS. The results for samples with higher Zr-doping levels (≥ 25%), which are not shown, all contained relatively high amount of low-conduction $LiTaO_3$ impurity and yielded very low ionic conductivities. The Nyquist plots of the impedances for $Li_{1.125}Ta_{0.875}Zr_{0.125}SiO_5$ (x=0.125) sample at variable temperatures are shown in **Figure 8**b. The impedance spectra show a semicircle in the high-frequency region followed by a spike at low-frequency region. The low-frequency spike represents the impedance response due to the blocking of mobile Li ions at the electrode interface, which is typical behavior for an ionic conductor. The ionic conductivities were calculated based on the total resistance (including bulk and grain boundary resistance) obtained from the intercept of the semicircle and the spike on the x-axis and the dimensions of the pellets. Arrhenius plot of the samples are shown in **Figure 8**a. The $\log(\sigma)$ versus $1/\mathrm{T}$ curves of the samples show good linearity, indicating no phase transition or ordering change within the measured temperature range. For the undoped $LiTaSiO_5$ sample, Nyquist plots can be obtained only above 100°C due to the large resistance and frequency limits. The ionic conductivity of $LiTaSiO_5$ is measured to be 1.47×10^{-6} S·cm^{-1} at 100°C. Based on the linear fitting of Arrhenius plots, the conductivity of $LiTaSiO_5$ at room temperature was estimated to be 3.11×10^{-8} S·cm^{-1} through extrapolation.

For 12.5% and 20% Zr-doped samples, Li^+ conductivity (σ) at 30°C was calculated to be 1.00×10^{-5} S·cm^{-1} and 3.9×10^{-6} S·cm^{-1}, respectively. Additional results of 5% and 10% Zr-doped samples can be found in the supporting information, including their XRD patterns (**Figure S10**), ionic conductivities, and activation energy (**Figure S9** and **Table S3**). Compared with undoped $LiTaSiO_5$ sample, the Zr-doped samples showed two to three orders of magnitude higher conductivity at room temperature. This can be explained by the additional Li^+ interstitial sites introduced by cation doping with lower valence and the resultant lower energy barrier potentially activated by these interstitial sites. The difference in ionic radii between Ta^{5+} (0.64 Å) and Zr^{4+} (0.72 Å) also gives rise to structure distortions and can possibly create more space to accommodate extra Li ions and facilitate faster Li^+ diffusion. It is also noteworthy that the room temperature conductivity of 12.5% Zr-doped sample (1.00×10^{-5} S·cm^{-1}) is lower than computational results (2.8×10^{-3} S·cm^{-1}), and more Zr-doping (20%) did not improve the conductivity but resulted in a lower value instead, which is opposite to the trend predicted computationally. Both observations are closely related to the formation of poorly conductive $Li_{1+x}Ta_{1-x}Zr_xO_3$ impurities. Higher Zr-doping level results in higher fraction of the $Li_{1+x}Ta_{1-x}Zr_xO_3$ phase, as shown in **Figure 5**a, which is detrimental to the percolation of the conducting $Li_{1+x}Ta_{1-x}Zr_xSiO_5$ phase through the pellet and therefore significantly lowers the measured overall conductivity. These two competing effects suggest that the optimal amount of Zr-doping to achieve the highest Li^+ conductivities should range between 10% and 20%, while the actual value will also depend on the synthesis and pressing conditions and can vary within a certain range.

Based on the linear fits of the Arrhenius plots in **Figure 8**, the diffusion activation energy can be calculated using the equation $\sigma = A\exp(-E_a/k_bT)$, where A is the pre-exponential parameter, E_a is the activation energy, and k_b is the Boltzmann constant. The results are listed in **Table 2**. From undoped samples to 12.5% Zr-doped $LiTaSiO_5$ samples, the activation energy decreases from 0.51 eV to 0.38 eV, while the 20% Zr-doped sample shows an activation energy of 0.43 eV higher than the 12.5% Zr-doped sample. As predicted, Zr-doping can effectively decrease the diffusion barriers and result in a lower activation energy than the undoped $LiTaSiO_5$ sample, although the activation energy is still higher than computational results (0.21 - 0.25 eV). This phenomenon, again, can be ascribed to the existence of the poorly conductive $Li_{1+x}Ta_{1-x}Zr_xO_3$ impurity. Among all the samples synthesized and tested experimentally, 12.5% Zr-doped sample ($Li_{1.125}Ta_{0.875}Zr_{0.125}SiO_5$) showed the lowest activation energy and the highest ionic conductivity, suggesting a significant improvement over the $LiTaSiO_5$ phase potentially due to the concerted migration with a lower energy barrier activated by the Zr^{4+} doping.

The electronic conductivities of the doped samples were evaluated with using DC polarization measurements. The DC electronic conductivities for 12.5% Zr and 20% Zr doped $LiTaSiO_5$ samples are estimated to be 3.23×10^{-9} $S{\cdot}cm^{-1}$ and 1.89×10^{-10} $S{\cdot}cm^{-1}$, respectively, and the Li ion transport numbers are both calculated to be close to 1.0 (>0.9997 and >0.9999, respectively). These results suggest that the doped materials are pure lithium ion conductors.

Cyclic voltammogram (CV) tests of these materials were also conducted (**Figure S11**). The results indicate that this compound is stable against most cathodes. Redox of Ta and Si may be activated at low voltage range, indicating protection mechanism need to be used when Li metal is used as the anode. An all-solid-state cell was also assembled to demonstrate the feasibility of this material as solid electrolyte. The cell with $LiFePO_4$ cathode, Li-In alloy anode and 12.5% Zr-doped sample as the electrolyte was successfully cycled at 80 °C and a reasonably good capacity was achieved (**Figure S12**). Optimizations are necessary to improve the rate capability, cycling stability, and reversible capacity of the cells. But for a new compound that was synthesized for the first time and not fully optimized, the successful cycling of the solid-state cell is encouraging and warrants more work on this class of materials in the future.

3. Discussion

In this integrated computational and experimental study, we designed a group of $Li_{1+x}Ta_{1-x}Zr_xSiO_5$ compounds based on a rational strategy of activating concerted migration to achieve higher ionic conductivity in a given crystal structure. This strategy is demonstrated by the successful synthesis of $Li_{1+x}Ta_{1-x}Zr_xSiO_5$ sphene compounds and the significant improvement of ionic conductivity by three orders of magnitude over the original sphene $LiTaSiO_5$. Although currently it is difficult to experimentally verify the concerted migration mechanism with known characterization techniques, this design strategy is demonstrated to be effective in realizing high conductivity in a number of known super ionic conductors, such as garnet LLZO, LGPS, and LATP,[13] and now in a newly discovered family of fast ionic conductors. The sphene structure has long been known but has not investigated for ion transport. The computationally predicted Zr-doping converts a non-conductive structure ($<10^{-8}$ S·cm^{-1}) to a highly conductive structure of 10^{-5} - 10^{-4} S·cm^{-1}, making this new family of compounds potential competitors to the known oxide super-ionic conductors such as LLZO.

In our experiments, the 12.5% Zr-doped sample showed a promising room-temperature conductivity of $>10^{-5}$ S·cm^{-1}. Since this is the first study on this new compound, the synthesis conditions are not yet optimized for this materials system. The existence of the ionic insulating impurity phases and the relatively low density of the pellet may be attributed as the main causes for the discrepancy between computation prediction and experiments. The measured conductivity was improved after hot-pressing compared to the results from the simply sintered pellets. Even after hot pressing, the density of the pellets was still relatively low, around 86-89%, because the size of the primary particle was large, and the morphology was irregular, which is a result of long-time high temperature synthesis. Investigations on other oxide conductors such as LLZO demonstrated that high conductivity can only be achieved when the pellet density is >99%.[21] The first study of lithium garnet reported an ionic conductivity of about 10^{-5} $S\cdot cm^{-1}$,[22] which is similar to the conductivity reported in this study of the lithium sphene structure. We believe the ionic conductivity of this lithium sphene family has great potential for future improvement and can be further increased to the level of computation prediction.

With more optimization in the synthesis processes, the purity of the synthesized materials can be improved, and this new family of sphene structure can be made in many different compounds. In addition to Zr-doping, a number of dopants were experimentally attempted. We selected Zr in this study because of its good integration as a dopant in this structure and decent electrochemical stability at both high and low voltages.[11-12] We found that the Ti^{4+} doped sphene phase can also form with a low solubility limit, but Ti may have poor reduction stability. Ga^{3+} and Sn^{4+} dopants were also tried and successfully yield the sphene phase as the major phase and various amounts of $LiTaO_3$-like phase as the secondary phase. Our novel computation-based design strategy distinguishes itself from conventional doping design or combinatorial design, because not every dopant can convert a structure into good ionic conductor, and combinatorial trials of aliovalent doping in experiments are time-consuming. The promising structures that may produce high conductivity can be effectively screened and identified by the computation integrated with topological analysis, DFT calculations, and AIMD simulations, as demonstrated in this study. This rational design strategy guided by first principles computation can potentially lead to the discovery of more promising fast ion conductors.

4. Conclusion

In this combined computational and experimental materials study, we identify and design the doped $LiTaSiO_5$ sphene compounds $Li_{1+x}Ta_{1-x}Zr_xSiO_5$ ($0.5 \geq x \geq 0$) as new Li-ion conductors As guided by our design strategies and first principles computation, we predicted that a modification of the LiTaSiO5 sphene structure, by Zr-to-Ta doping and Li insertion, would activate the concerted migration of multiple Li ions, thereby significantly enhancing the ionic conductivity. These computation-predicted materials were successfully synthesized and confirmed in experiments. With a doping level of 12.5% Zr, $Li_{1.125}Ta_{0.875}Zr_{0.125}SiO_5$ showed a total ionic conductivity of approximately 10^{-5} S·cm^{-1} at 30°C, which is three orders of magnitude higher than the undoped $LiTaSiO_5$. Our study uncovers the sphene as a new structure of the fast Li^+ conductor family. More importantly, the sphene family includes many chemical compositions and expands the space for future materials design of new Li-ion conductors. Further exploration of this new sphene structure is promising for achieving even higher conductivities. Finally, our combined computational and experimental study demonstrates the rational design strategy of activating concerted migration for fast ion conductors and serves as an example for future materials design of fast ion conductor materials.

5. Methods

5.1 Computational methods

In this study, all density functional theory (DFT) calculations were performed using the Vienna *Ab initio* Simulation package (VASP)[23] within the projector augmented-wave approach with Perdew-Burke-Ernzerhof (PBE)[24] generalized-gradient approximation (GGA). The materials entries for the phase diagram were obtained from the *Materials Project* (MP)[25-27] database and convergence parameters in all static DFT calculations are consistent to MP. The density of states (DOS) were calculated using the Heyd-Scuseria-Erznerhof (HSE) functional with Monkhorst-Park $2 \times 2 \times 2$ *k*-point grid. We evaluated the phase stability and chemical stability of $Li_{1+x}Ta_{1-x}Zr_xSiO_5$ using the same scheme in our previous work.[19, 28]

Li site and Structure: We performed topological analysis of the $LiTaSiO_5$ crystal structural framework to identify the potential Li sites. The topological analysis was performed using the Voronoi-Dirichlet partition algorithm implemented in *Zeo++* [29, 30] on the $LiTaSiO_5$ crystal structural framework with all Li removed and with the crystal ionic radius of ion species in the analysis.[31] The Voronoi nodes obtained from the Voronoi-Dirichlet partition of the non-Li structural framework correspond to the center of local void space that may occupy a Li ion. For $Li_{1+x}Ta_{1-x}Zr_xSiO_5$, we used the extra Li sites determined by topological analysis and substituted Ta with Zr. A $\left(\sqrt{3}/2 \times 1 \times 1\right)\mathrm{R}30°$ supercell model with eight formula unit was used for doped compositions (Table S2). Using *pymatgen*, we generated 50 symmetrically distinctive structures. All these structures were statically relaxed in the DFT calculations, and the structure with the lowest DFT energy was identified as the ground state structure for other calculations.

Phase Stability: We evaluated the phase stability of the doped compositions using the same scheme in references.[32, 33] The phase stability is measured by the 'energy above hull' as the decomposition energy to the thermodynamic phase equilibria.[11] The energy above hull ΔE of $Li_{1+x}Ta_{1-x}Zr_xSiO_5$ was evaluated using *pymatgen* based on the DFT energies from the *Materials Project*.[18] The electrochemical window is evaluated using the grand potential phase diagrams as in the previous study.[10]

Li-ion Diffusion: We performed *ab initio* molecular dynamic (AIMD) simulations to investigate the Li diffusional properties. We used the setting of a Γ-centered *k*-point in the non-spin-polarized DFT calculations. The time step was set to 2 fs. During the estimation of Li ion diffusion, NVT ensemble using Nosé-Hoover thermostat[34] was adopted. The total time of AIMD simulations were in the range of 100 ps to 600 ps until the diffusivity was converged. The ionic conductivity and their error bars were calculated following established methods in previous studies.[35]

5.2 Experimental methods

Synthesis of $Li_{1+x}Ta_{1-x}Zr_xSiO_5$: The $Li_{1+x}Ta_{1-x}Zr_xSiO_5$ (x=0, 0.125, 0.2, 0.25, 0.3, 0.5) samples were synthesized by solid state reactions. Starting materials including Li_2CO_3(Alfa Aesar, 99.0%), Ta_2O_5(Sigma Aldrich, 99.5%), ZrO_2(Alfa Aesar, 99.5%) and SiO_2(Alfa Aesar, 99.5%) were weighed and mixed with the stoichiometric ratios of the designed formulas. Li_2CO_3 was used in 10% excess to compensate the loss of lithium during heating. The mixture was ball-milled at 500 rpm for 1 hour and then pressed into pellets with a diameter of 0.5 inch. Each pellet is about 0.5 g. The pellets were calcinated in alumina boats at 1100°C for 45 hours, followed by quenching on a copper plate in air to room temperature. The synthesized pellets and powder were stored in an Ar filled glove box to avoid exposure to moisture.

Characterization: Crystal structures of the obtained samples were analyzed by X-Ray Diffraction (XRD) with using a D8 Advance X-ray Diffractometer (Bruker) equipped with a LynxEye detector and a Molybdenum tube ($\lambda\ \mathrm{K}\alpha_1 = 0.7093$ Å). The samples were scanned in an air-tight sample container covered with a Kapton tape to avoid exposure to air and moisture. High resolution synchrotron XRD data was also collected at beam line 17-BM at the Advanced Photon Source (APS) at the Argonne National Laboratory (ANL). Rietveld refinement was performed on the synchrotron XRD data with the EXPGUI suite of GSAS code.[36]

To investigate the reaction pathway in the synthesis process, *in situ* XRD was conducted on various $Li_{1+x}Ta_{1-x}Zr_xSiO_5$ (x=0, 0.2 and 0.5) pellets using an Anton Paar HTK1200N furnace installed on the D8 Advance diffractometer. For x = 0 and 0.2 samples, the temperature profile includes a ramping process (30°C/min) from room temperature to 1050°C with multiple intermediate temperature holding steps. XRD patterns were collected first at 50°C, then at each constant temperature from 450°C to 1050°C with a step size of 50°C. After being held at 1050°C for 4 hours, the chamber was cooled down to room temperature and another two XRD patterns were collected at 600°C and 100°C. For the sample with x = 0.5, a similar ramping program was adopted with holding at a highest temperature of 1150°C for 4 hours to facilitate the doping of more Zr.

Electrochemical Tests: Electrochemical Impedance Spectroscopy (EIS) was used to determine the Li ion conductivity of the samples. The AC impedance measurements were performed using a Bio-Logic VMP3 impedance analyzer in the frequency range from 1 MHz to 0.5 Hz with a voltage amplitude of 300mV. Temperature-dependent conductivity measurements were performed from room temperature to 150°C (200°C for $LiTaSiO_5$) using two stainless-steel rods as ion-blocking electrodes.[37] To perform the measurements, pellets of 0.5-inch diameter and ~1.5 mm thickness were obtained by sintering nano/micro powder using a direct current-induced hot press with uniaxial pressure of 1 ton. The samples were heated up at a rate of 100 °C/min to 1100-1150 °C, maintained for 2 minutes and cooled naturally to room temperature in air. The relative density of the sintered pellets is calculated by carefully measuring the dimensions of the well-shaped pellets and their masses.

The electronic conductivity of the doped samples was evaluated through DC polarization measurements. Symmetric cells with two stainless steel (SS) rods as blocking electrodes and the doped samples $Li_{1+x}Ta_{1-x}Zr_xSiO_5$ (or LTZSO, x=0.125 and 0.20) as electrolyte were assembled, represented as SS|LTZSO|SS. A voltage of 0.75 V is applied to the cells. The currents are recorded and the stable currents are used to calculate DC electron conductivities.

Supporting Information

Supporting Information is available from the Wiley Online Library or from the author.

Acknowledgements

S.X., X.H., and A.H. contributed equally to this work. X.H, and Y.M. acknowledge the finical support by acknowledge the support from National Science Foundation under award No. 1550423 and the computational facilities from the University of Maryland supercomputing resources, the Maryland Advanced Research Computing Center (MARCC), and the Extreme Science and Engineering Discovery Environment (XSEDE) supported by National Science Foundation Award No. DMR150038. S.X and H.C. acknowledge the finical support by the U.S. National Science Foundation under grant numbers DMR-1605692 and CBET-1706723. The use of the Advanced Photon Source and the National Synchrotron Light Source II were supported by the U.S. Department of Energy, Office of Science, through the general user programs. A portion of this research used resources at the Spallation Neutron Source (SNS), a DOE Office of Science User Facility operated by the Oak Ridge National Laboratory. S.X and H.C. acknowledge Dr. Peter Hesketh for the help on EIS measurements.

Received: ((will be filled in by the editorial staff))
Revised: ((will be filled in by the editorial staff))
Published online: ((will be filled in by the editorial staff))

Reference

[1] J.C. Bachman, S. Muy, A. Grimaud, H.-H. Chang, N. Pour, S.F. Lux, O. Paschos, F. Maglia, S. Lupart, P. Lamp, L. Giordano, and Y. Shao-Horn, *Chemical Reviews*, **2016**. *116*, 140.

[2] Y. Wang, W.D. Richards, S.P. Ong, L.J. Miara, J.C. Kim, Y. Mo, and G. Ceder, *Nature Materials*, **2015**. *14*, 1026.

[3] J. Janek and W.G. Zeier, *Nature Energy*, **2016**. *1*, 16141.

[4] K.H. Park, Q. Bai, D.H. Kim, D.Y. Oh, Y. Zhu, Y. Mo, and Y.S. Jung, *Advanced Energy Materials*, **2018**. *8,* 1800035.

[5] N. Kamaya, K. Homma, Y. Yamakawa, M. Hirayama, R. Kanno, M. Yonemura, T. Kamiyama, Y. Kato, S. Hama, K. Kawamoto, and A. Mitsui, *Nat Mater*, **2011**. *10*, 682.

[6] Y. Seino, T. Ota, K. Takada, A. Hayashi, and M. Tatsumisago, *Energy Environ. Sci.*, **2014**. *7*, 627.

[7] V. Thangadurai, S. Narayanan, and D. Pinzaru, *Chem Soc Rev*, **2014**. *43*, 4714.

[8] R. Murugan, V. Thangadurai, and W. Weppner, *Angew Chem Int Ed Engl*, **2007**. *46*, 7778.

[9] H. Aono, E. Sugimoto, Y. Sadaoka, N. Imanaka, and G.-y. Adachi, *Solid State Ionics*, **1990**. *40-41*, 38.

[10] Y. Zhu, X. He, and Y. Mo, *ACS Applied Materials & Interfaces*, **2015**. *7*, 23685.

[11] A.M. Nolan, Y. Zhu, X. He, Q. Bai, and Y. Mo, *Joule*, **2018**. *2*, 2016.

[12] Y. Zhu, X. He, and Y. Mo, *Adv Sci (Weinh)*, **2017**. *4*, 1600517.

[13] X. He, Y. Zhu, and Y. Mo, *Nature Communications*, **2017**. *8*, 15893.

[14] K. Arbi, J.M. Rojo, and J. Sanz, *Journal of the European Ceramic Society*, **2007**. *27*, 4215.

[15] W.H. Zachariasen, *Z. Kristallogr.*, **1930**. *73*, 7.

[16] L. Sebastian, J. Gopalakrishnan, and Y. Piffard, *Journal of Materials Chemistry*, **2002**. *12*, 374.

[17] E.A. Genkina and B.V. Mill, *Kristallografiya*, **1992**. *37*, 1424.

[18] A. Jain, S.P. Ong, G. Hautier, W. Chen, W.D. Richards, S. Dacek, S. Cholia, D. Gunter, D. Skinner, G. Ceder, and K.A. Persson, *APL Materials*, **2013**. *1*.

[19] Y. Mo, S.P. Ong, and G. Ceder, *Chemistry of Materials*, **2012**. *24*, 15.

[20] D.A. Weber, A. Senyshyn, K.S. Weldert, S. Wenzel, W. Zhang, R. Kaiser, S. Berendts, J. Janek, and W.G. Zeier, *Chemistry of Materials*, **2016**. *28*, 5905.

[21] F. Han, J. Yue, C. Chen, N. Zhao, X. Fan, Z. Ma, T. Gao, F. Wang, X. Guo, and C. Wang, *Joule*, **2018**. *2*, 497.

[22] V. Thangadurai, H. Kaack, and W.J.F. Weppner, *Journal of American Ceramic Society*, **2004**. *86*.

[23] G. Kresse and J. Furthmuller, *Physical Review B*, **1996**. *54*, 11169.

[24] J.P. Perdew, M. Ernzerhof, and K. Burke, *The Journal of Chemical Physics*, **1996**. *105*, 9982.

[25] A. Jain, G. Hautier, C.J. Moore, S. Ping Ong, C.C. Fischer, T. Mueller, K.A. Persson, and G. Ceder, *Computational Materials Science*, **2011**. *50*, 2295.

[26] A. Jain, G. Hautier, S.P. Ong, C.J. Moore, C.C. Fischer, K.A. Persson, and G. Ceder, *Physical Review B*, **2011**. *84*, 045115.

[27] A. Jain, S.P. Ong, G. Hautier, W. Chen, W.D. Richards, S. Dacek, S. Cholia, D. Gunter, D. Skinner, G. Ceder, and K.A. Persson, *APL Materials*, **2013**. *1*, 011002.

[28] X. He and Y. Mo, *Physical chemistry chemical physics : PCCP*, **2015**. *17*, 18035.

[29] T.F. Willems, C.H. Rycroft, M. Kazi, J.C. Meza, and M. Haranczyk, *Microporous and Mesoporous Materials*, **2012**. *149*, 134.

[30] R.L. Martin, B. Smit, and M. Haranczyk, *J Chem Inf Model*, **2012**. *52*, 308.

[31] R.D. Shannon, *Acta crystallographica section A: crystal physics, diffraction, theoretical and general crystallography*, **1976**. *32*, 751.

[32] X. He and Y. Mo, *Phys Chem Chem Phys*, **2015**. *17*, 18035.

[33] S.P. Ong, Y. Mo, W.D. Richards, L. Miara, H.S. Lee, and G. Ceder, *Energy Environ. Sci.*, **2013**. *6*, 148.

[34] S. Nose, *Progress of Theoretical Physics Supplement*, **1991**. *103*, 1.

[35] X. He, Y. Zhu, A. Epstein, and Y. Mo, *npj Computational Materials*, **2018**. *4*, 18.

[36] B.H. Toby, *Journal of Applied Crystallography*, **2001**. *34*.

[37] S. Xiong, Z. Liu, H. Rong, H. Wang, M. McDaniel, and H. Chen, *Sci Rep*, **2018**. *8*, 9146.

[38] X. He, Y. Zhu, A. Epstein, and Y. Mo, *npj Computational Materials*, **2018**. *4*.

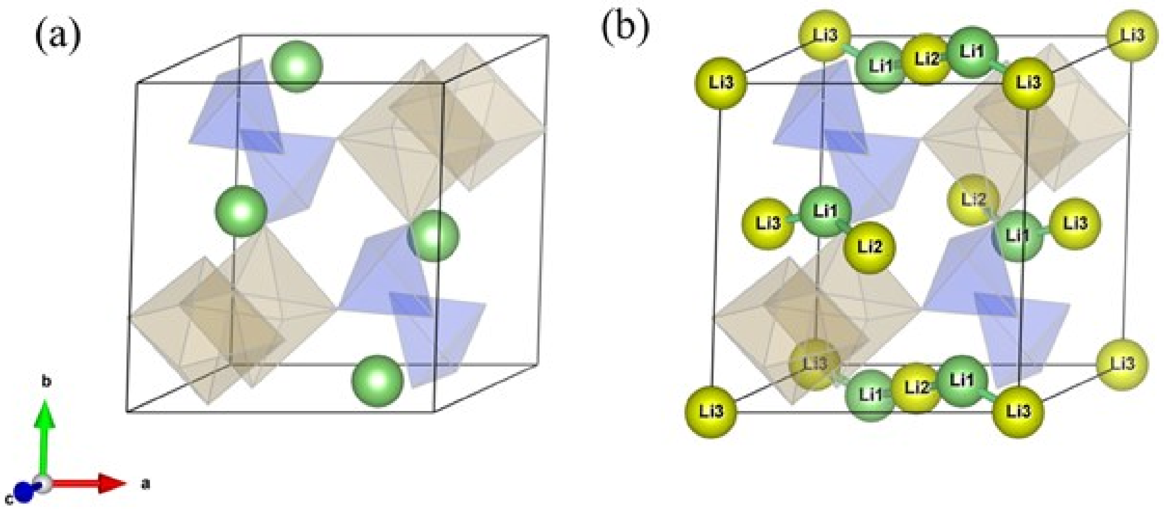

Figure 1. (a) Experimental crystal structures of $LiTaSiO_5$, and (b) Crystal structure of $LiTaSiO_5$ with the experimental Li site (Li1) and computationally predicted additional interstitial sites Li2 and Li3 for extra Li (shown as yellow spheres). TaO_6 and SiO_4 are shown as brown and blue polyhedrons, respectively. Green bars represent the connection between these Li sites.

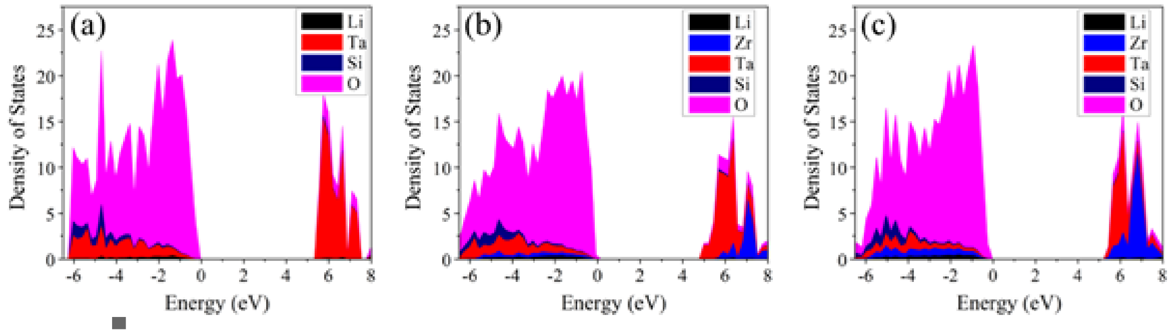

Figure 2. Calculated density of states for (a) $LiTaSiO_5$, (b) $Li_{1.25}Ta_{0.75}Zr_{0.25}SiO_5$, and (c) $Li_{1.5}Ta_{0.5}Zr_{0.5}SiO_5$ using HSE functional.

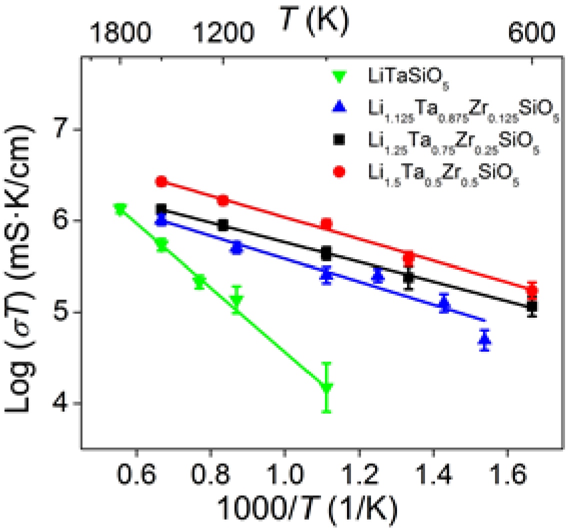

Figure 3. Arrhenius plots of Li^+ diffusion in $Li_{1+x}Ta_{1-x}Zr_xSiO_5$ (x = 0, 0.125, 0.25, and 0.5) from AIMD simulations. The error bar is estimated using the scheme in ref.[38]

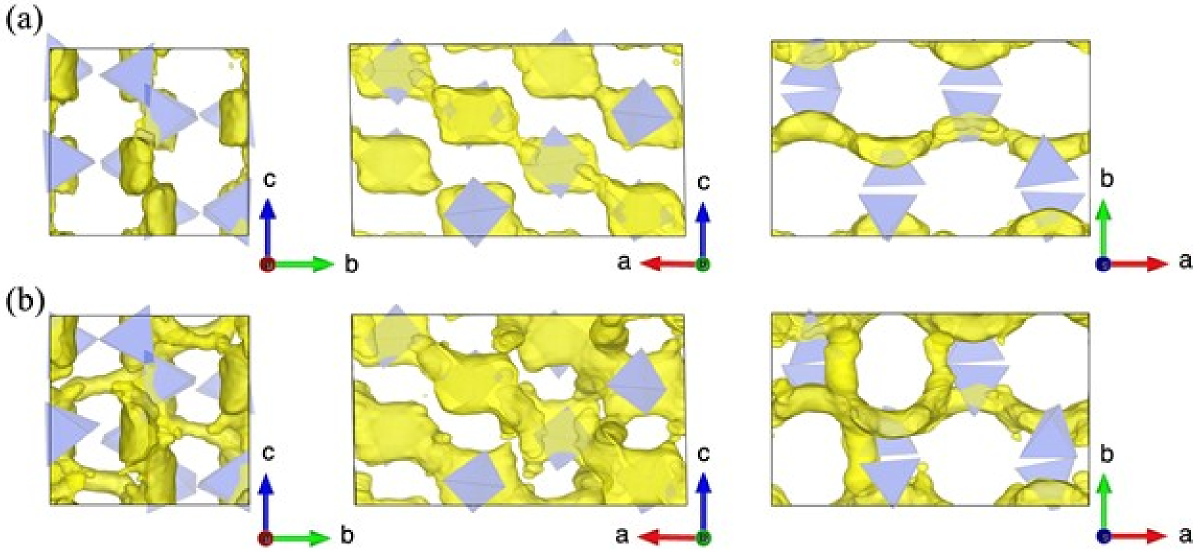

Figure 4. The probability density of Li ions spatial occupancy during AIMD simulations in (a) $LiTaSiO_5$ and (b) $Li_{1.25}Ta_{0.75}Zr_{0.25}SiO_5$, in different perspective. The isosurface is plotted at the mean value of

the probability density in each structure over the entire AIMD simulation. Only SiO_4 polyhedrons (blue) are shown for clarity.

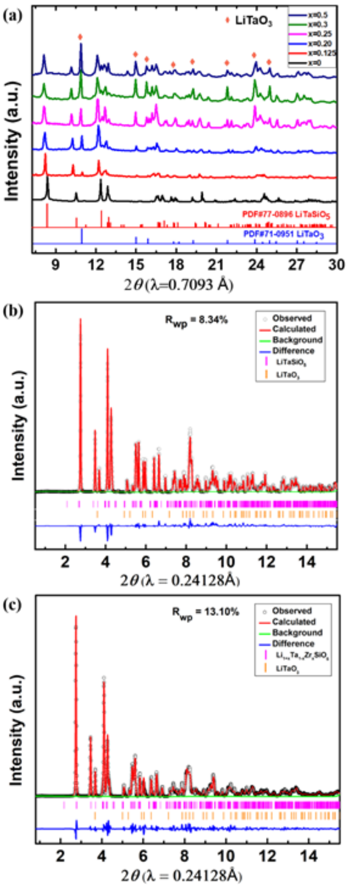

Figure 5. (a) The XRD patterns of as-synthesized $Li_{1+x}Ta_{1-x}Zr_xSiO_5$ samples for x=0, 0.125, 0.2, 0.25, 0.3 and 0.5. (b) XRD pattern and Rietveld refinement of $LiTaSiO_5$ (x=0) sample. (c) XRD pattern and Rietveld refinement of $Li_{1.125}Ta_{0.875}Zr_{0.125}SiO_5$ (x=0.125) sample.

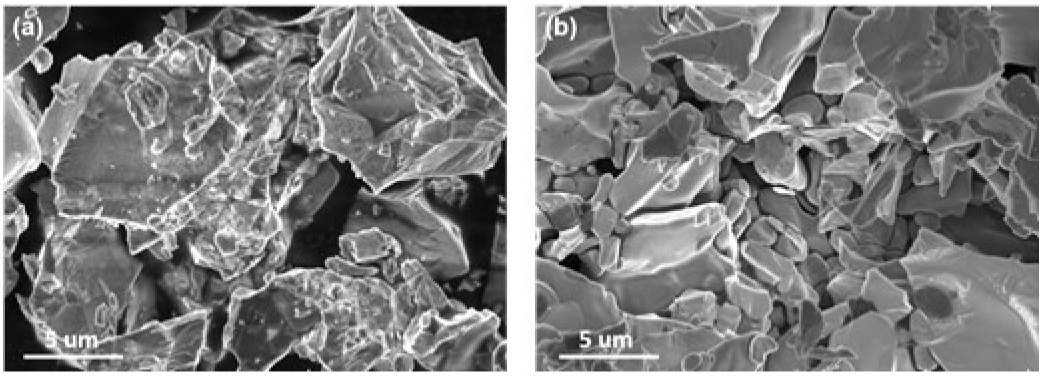

Figure 6. SEM images of $Li_{1.125}Ta_{0.875}Zr_{0.125}SiO_5$ (x=0.125) sample in the forms of (a) powder and (b) hot-pressed pellet.

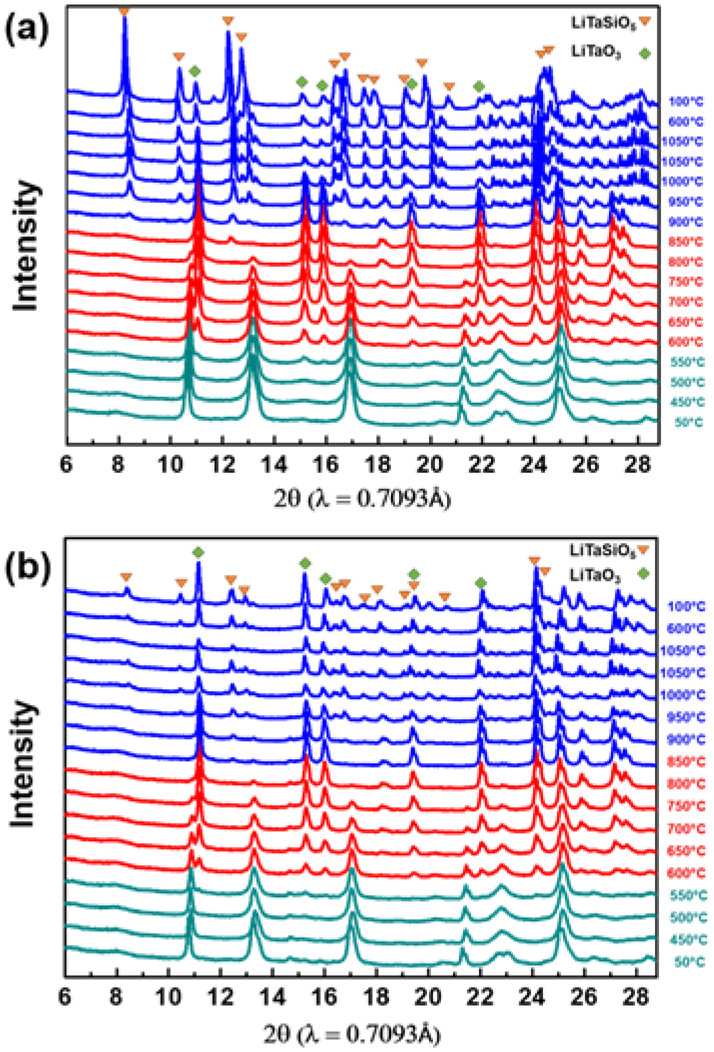

Figure 7. In situ XRD pattern of $Li_{1+x}Ta_{1-x}Zr_xSiO_5$ samples with various Zr-doping levels. (a) $LiTaSiO_5$ (x=0), (b) $Li_{1.2}Ta_{0.8}Zr_{0.2}SiO_5$ (x=0.2).

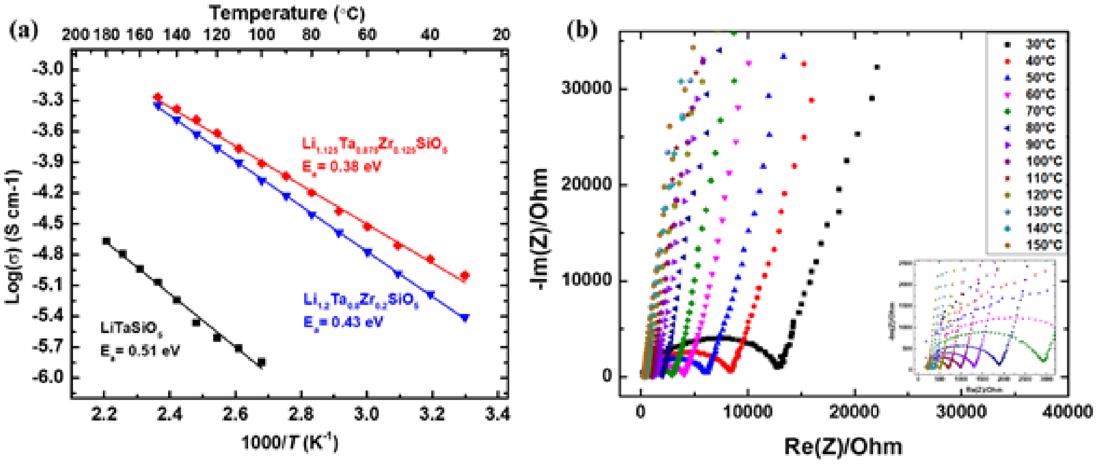

Figure 8. (a) Arrhenius plots of $Li_{1+x}Ta_{1-x}Zr_xSiO_5$ for x = 0, 0.125, and 0.2, corresponding to 0%, 12.5%, and 20% Zr doped $LiTaSiO_5$ samples. (b) Nyquist impedance plots of $Li_{1.125}Ta_{0.875}Zr_{0.125}SiO_5$ (x=0.125) from 30°C to 150°C (the inset shows the zoomed-in region for details at higher temperatures).

Table 1. Diffusional properties and phase stability of $Li_{1+x}Ta_{1-x}Zr_xSiO_5$. Error bar of the ionic conductivity is estimated based on the error bars of E_a and D obtained during the linear fitting using the scheme in ref. [38]

Composition	Energy above hull (meV/atom)	E_a (eV)	σ at 300 K (mS·cm^{-1})	Error bound [σ_{min} ,σ_{max}] (mS·cm^{-1})
$LiTaSiO_5$	0	0.70 ± 0.06	7.6×10^{-7}	[8.0×10^{-8}, 7.3×10^{-6}]
$Li_{1.125}Ta_{0.875}Zr_{0.125}SiO_5$	11	0.25 ± 0.02	1.5	[0.7, 3.5]
$Li_{1.25}Ta_{0.75}Zr_{0.25}SiO_5$	15	0.21 ± 0.02	6.1	[2.6, 14.0]
$Li_{1.5}Ta_{0.5}Zr_{0.5}SiO_5$	28	0.23± 0.02	6.3	[3.3, 12.0]

Composition	E_a (eV)	Ionic conductivity at 30°C (mS·cm^{-1})
$LiTaSiO_5$	0.51 eV	3.11×10^{-5} (extrapolated)
$Li_{1.125}Ta_{0.875}Zr_{0.125}SiO_5$	0.38 eV	0.010
$Li_{1.2}Ta_{0.8}Zr_{0.2}SiO_5$	0.43 eV	0.0039

Table 2. Activation energy and ionic conductivity (30°C) of $Li_{1+x}Ta_{1-x}Zr_xSiO_5$ for x=0, 0.125, and 0.2.

Table of Contents

Computation Guided Design of $LiTaSiO_5$, a New Lithium Ionic Conductor with Sphene Structure

Shan Xiong, Xingfeng He, Aijie Han, Zhantao Liu, Zhensong Ren, Brian McElhenny, Adelaide M Nolan, Shuo Chen*, Yifei Mo*, and Hailong Chen*

A group of lithium oxosilicates with sphene structure, $Li_{1+x}Ta_{1-x}Zr_xSiO_5$ (x = 0-0.2), a new family of fast lithium ion-conducting solid electrolytes for all-solid-state lithium-ion batteries, was successfully identified, synthesized, and demonstrated in this joint computational and experimental study. High room-temperature ionic conductivity of $>10^{-5}$ S·cm^{-1} was achieved along with good stability and electrochemical performance.